Correspondence to:
C. Norgren,
cecilia.norgren@uib.no

Electron Acceleration and Thermalization at Magnetotail Separatrices

C. Norgren[1] [ID], M. Hesse[1,2] [ID], D. B. Graham[3] [ID], Yu. V. Khotyaintsev[3] [ID], P. Tenfjord[1] [ID], A. Vaivads[4] [ID], K. Steinvall[3,5] [ID], Y. Xu[6] [ID], D. J. Gershman[7,8] [ID], P.-A. Lindqvist[4] [ID], F. Plaschke[9] [ID], and J. L. Burch[2] [ID]

[1]Space Plasma Physics Group, University of Bergen, Bergen, Norway, [2]Southwest Research Institute, San Antonio, TX, USA, [3]Swedish Institute of Space Physics, Uppsala, Sweden, [4]Space and Plasma Physics, School of Electrical Engineering, KTH Royal Institute of Technology, Stockholm, Sweden, [5]Space and Plasma Physics, Department of Physics and Astronomy, Uppsala University, Uppsala, Sweden, [6]School of Space and Environment, Beihang University, Beijing, China, [7]NASA Goddard Space Flight Center, Greenbelt, MD, USA, [8]Department of Astronomy, University of Maryland, College Park, MD, USA, [9]Space Research Institute, Austrian Academy of Sciences, Graz, Austria

Abstract In this study we use the Magnetospheric Multiscale mission to investigate the electron acceleration and thermalization occurring along the magnetic reconnection separatrices in the magnetotail. We find that initially cold electron lobe populations are accelerated toward the X line forming beams with energies up to a few kiloelectron volts, corresponding to a substantial fraction of the electron thermal energy inside the exhaust. The accelerated electron populations are unstable to the formation of electrostatic waves which develop into nonlinear electrostatic solitary waves. The waves' amplitudes are large enough to interact efficiently with a large part of the electron population, including the electron beam. The wave-particle interaction gradually thermalizes the beam, transforming directed drift energy to thermal energy.

1. Introduction

Magnetic reconnection is a universal process where magnetic energy is often explosively released, leading to particle acceleration and heating. Observations suggest that magnetic reconnection and subsequent processes can accelerate electrons to energies of tens or even hundreds of kiloelectron volts (e.g., Fu et al., 2019; Hoshino et al., 2001; Øieroset et al., 2002; Vaivads et al., 2011). The particle energization associated with magnetic reconnection is known to take place in several regions: in the inflow region and along the separatrices (e.g., Egedal et al., 2008; Eriksson et al., 2018; Hesse, Norgren, et al., 2018; Nagai et al., 2001), inside the ion and electron diffusion regions (e.g., Hesse, Liu, et al., 2018; Khotyaintsev et al., 2020; Torbert et al., 2018; Wang et al., 2018), in the magnetic reconnection exhaust (e.g., Bessho et al., 2015; Eriksson et al., 2020), in the vicinity of magnetic islands (Chen et al., 2008; Huang et al., 2012), both during island coalescence (Pritchett, 2008) and contraction (Drake et al., 2006), and at dipolarization fronts (e.g., Fu et al., 2011; Vaivads et al., 2011). Where, how, and to what extent the particles are accelerated depend not only on fundamental properties such as the particle species and the relative composition of species but also on changing properties, such as the particle's velocity. Two examples of the former are that the presence of heavier ions or cold ionospheric ions can act as energy sinks in addition to reducing the rate at which magnetic flux is being reconnected (e.g., Tenfjord et al., 2019; Toledo-Redondo et al., 2017). One example of the latter is Fermi acceleration in the reconnection exhaust or in magnetic islands where the energization is more efficient if the initial velocity is higher (Drake et al., 2006; Northrop, 1963). A clear indication of the non-uniform energization of a particle species is the fact that the energy partition is generally not uniform, with some particles being accelerated to superthermal energies, while some remain thermal (e.g., Hoshino et al., 2001). How this energy-dependent energization affects the bulk energization of a species is unclear. For example, a study of the change in electron temperature between the magnetosheath and the reconnection exhaust during reconnection at the dayside magnetopause did not show any strong dependence on the initial electron temperature in the magnetosheath (Phan et al., 2013). The acceleration mechanisms can vary between direct acceleration by electric fields, for example, the reconnection electric field inside the diffusion regions (Bessho et al., 2015), the already mentioned Fermi acceleration (Fermi, 1949), and betatron acceleration

(e.g., Northrop, 1963). Ultimately, due to the conservation of energy, the final plasma energies must depend on the amount of available magnetic energy compared to the amount of plasma to be reconnected, which varies during the reconnection process (Ergun et al., 2018; Vaivads et al., 2011).

In addition, energy transfer does not always occur directly between the magnetic field and the particles, but often in steps, between different plasma populations, mediated by electromagnetic fields. One such example is the Hall magnetic fields, which are due to the different motions of ion and electrons. Observations from the terrestrial magnetotail show that at the separatrices of magnetic reconnection, lower-energy field-aligned electrons flow into the reconnection region while higher-energy electrons flow out of the reconnection region (Asano et al., 2008; Nagai et al., 2001; Øieroset et al., 2001) carrying the outward and inward Hall currents, respectively (Nagai et al., 2003). The acceleration leading to the formation of these electron flows and associated currents has by some authors been suggested to be a necessity to maintain quasi-neutrality inside the ion diffusion region (Egedal et al., 2008; Uzdensky & Kulsrud, 2006). It has been explained as following: Inside the ion diffusion region, the demagnetized ions are free to move across the magnetic field while the magnetized electrons are tightly bound to the magnetic field lines. As a magnetic flux tube expands while convecting inward, the ion density can thus remain close to constant while the electron density must decrease. The resulting charge separation produces an electric field that accelerates electrons inward, which can lead to the formation of beams and temperature anisotropies (Egedal et al., 2005). In some cases, the electric field can become localized leading to the formation of double layers (Egedal et al., 2015; Ergun et al., 2009; Wang et al., 2014). The ultimate effect of electron acceleration along the separatrices remains disputed. For example, Bessho et al. (2015) found that the separatrix acceleration occurring at the inbound leg of an electron trajectory was mostly negated by the decelerating effect when the same electron arrived close to the separatrix on the opposite side of the neutral sheet. Meanwhile, Egedal et al. (2015) argued that the confining nature of the potential could lead to more efficient energization within the exhaust by the reconnection electric field. Furthermore, as mentioned above, an initially higher electron velocity would also lead to more efficient Fermi acceleration.

On a more local scale, electromagnetic waves can mediate energy transfer between different plasma populations. For example, the counter-streaming hot and cold electron populations occurring at reconnection separatrices have been studied extensively with numerical simulations. They have been shown to be unstable to the generation of electrostatic waves, leading to the thermalization of the cold electron beam (Chen et al., 2015; Divin et al., 2012; Egedal et al., 2015; Fujimoto, 2014; Huang et al., 2014). Depending on the velocity at which the waves are generated, they can interact with different parts of the electron distributions (Graham et al., 2015; Omura et al., 1996) and transfer energy between them. In the nonlinear stages of instabilities, it is common that electron trapping by the strong wave potential leads to the formation of electron phase space holes (EHs) and electrostatic solitary waves (ESWs) (e.g., Mozer et al., 2018). At reconnection separatrices, the interface between the inflowing and outflowing electrons represents a velocity shear. In such an environment, the instabilities developing may lead to transfer of energy not only between different energy ranges but also across the boundary (Hesse, Norgren, et al., 2018). Although electrostatic waves and ESWs are commonly observed at reconnection separatrices in conjunction with electron beams (Cattell et al., 2005; Viberg et al., 2013) or plateau distributions associated with significant drift speed (Ergun, Carlson, McFadden, Mozer, Muschietti, et al., 1998), their effect on plasma populations has not been firmly established.

In order to determine the importance of the separatrix acceleration and subsequent wave-particle interaction for the overall electron energization during magnetic reconnection, it is necessary to observe these phenomena in space. In this study we will do so, using high-cadence plasma and field measurements by the four closely separated Magnetospheric Multiscale (MMS) mission spacecraft. We are able to make detailed measurements of both the electron acceleration and subsequent wave-particle interaction at separatrix regions in the magnetotail.

2. Observations

In this section, we report MMS observations from the plasma sheet boundary layer. The electric field is from the Electric field Double Probes (EDP) (Ergun et al., 2014; Lindqvist et al., 2014), the magnetic field is from the FluxGate Magnetometer (FGM) (Russell et al., 2014), and the plasma distributions and moments are

from the Fast Plasma Investigation (FPI) (Pollock et al., 2016). All times are given in Coordinated Universal Time (UTC). Unless otherwise stated, positions and vectors are given in Geocentric Solar Ecliptic (GSE) coordinates.

We will first present observations of relatively thin channels of electron jets directed opposite to the broader ion and electron flows that is the exhaust flow of magnetic reconnection. For a few events, we will quantify the level of acceleration and compare it to the thermal energy of the lobe population and the plasma sheet population. We will then investigate the wave activity within these regions of accelerated electrons to infer the wave-particle interaction. We focus on electrostatic waves that propagate predominantly along the ambient magnetic field.

3. Electron Acceleration Channels

In this section we present an event from the magnetotail observed on 6 July 2017 at $[-18, 4, 2]$ Earth radii, investigated previously by Huang et al. (2019). Figure 1a shows the electron differential energy flux (DEF), in which we can identify the lobe at lower energies ($E_e \lesssim 1\,\text{keV}$) and the plasma sheet at higher energies ($E_e \gtrsim 1\,\text{keV}$). The spacecraft are initially located in the southern lobe before they enter the plasma sheet boundary layer and the outer edges of the plasma sheet. The spacecraft make partial exits into the lobe two more times before residing in the plasma sheet until the end of the displayed time interval. During this time, the magnetic field is predominantly tailward ($B_x < 0$). However, at 00:54:20 when the spacecraft encounters the plasma sheet for the first time, a significant northward component ($B_z > 0$) appears, closely associated with changes in B_x and B_y. Huang et al. (2019) interpreted this as a passing flux rope. The ion flow is Earthward ($v_{ix} > 0$), indicating that the spacecraft are located in the Earthward exhaust of a magnetic reconnection X line. We note that although v_{ix} maximizes at ∼800 km/s during the shown interval, the ion distribution consists of two populations: one cold population with bulk speed close to $v_{ix} = 0\,\text{km/s}$ and another hotter population streaming Earthward at speeds reaching >1,000 km/s (Figure 1d). In comparison, the Alfvén speed based on the lobe field $B = 20\,\text{nT}$ and the density $n = 0.1\,\text{cm}^{-3}$ is 1,400 km/s. At later times (not shown), the ion flow reverses, indicating that the X line is moving Earthward. Since we do not observe any reconnection outflow reversals in the immediate proximity of the acceleration channels, we have no straightforward means of determining how far away from the X line the spacecraft are located. However, velocity dispersion signatures in the reduced ion distribution (Figure 1d) suggest intermittent and sometimes approaching acceleration regions. In Figure 1d we mark two of those signatures in which ions with higher velocities are observed before ions with lower velocities (black lines). For both cases, the ions with lowest velocities ($v_{i,x} \rightarrow 0\,\text{km/s}$) are observed close to the two regions with enhanced B_z, which suggests that these locations are the regions of acceleration (injection points). These regions of enhanced B_z may correspond to dipolarization fronts, which are well-known regions of ion acceleration (e.g., Eastwood et al., 2015). Based on the velocity dispersion marked by the first black line, we estimate a distance to the injection point of about 1,500 km. The region where $v_{i,x} \rightarrow 0\,\text{km/s}$ appears about 1–2 s after, which suggests that the acceleration region or injection point approaches with a velocity of 750 to 1,500 km/s. Although the close spacecraft separation of about 15 km makes it difficult to decide the propagation velocity of larger-scale structures accurately, based on the time delay of the B_z enhancements among the four spacecraft, we estimate this structure to be moving at a speed $\gtrsim 1,000\,\text{km/s}$. This speed is consistent with the estimated propagation speed of the acceleration regions/injection points from the velocity dispersions and therefore supports the picture that the regions of enhanced B_z are the regions of ion acceleration. For the second marked dispersion signature the accelerated ion population is much weaker, likely because the spacecraft are located further toward the lobes. The two segments of the black line indicate that the distance to the injection point decreases from 8,500 to 1,000 km. Whether the regions of enhanced B_z correspond to dipolarization fronts, islands, or a combination thereof, they are all signatures of magnetic reconnection.

The Earthward ion flow is matched by an Earthward electron flow ($v_{ex} > 0$) (Figure 1e). In addition, at the edges of the Earthward flow, three shorter intervals of larger amplitude tailward ($v_{ex} < 0$) flows are observed. The electron flows are consistent with the current derived from the magnetic field (not shown). These regions are associated with density cavities where $n_e \sim 0.01\,\text{cm}^{-3}$ (Figure 1f). In comparison, the density in the lobe (before 00:54:10) is $n_e^{lb} \sim 0.05\,\text{cm}^{-3}$, and the largest density during the interval, which we associate with a plasma sheet population, is $n_e^{sh} \sim 0.15\,\text{cm}^{-3}$. The width of the density cavity is about twice that of the electron flow. This is consistent with numerical simulations of guide-field reconnection at
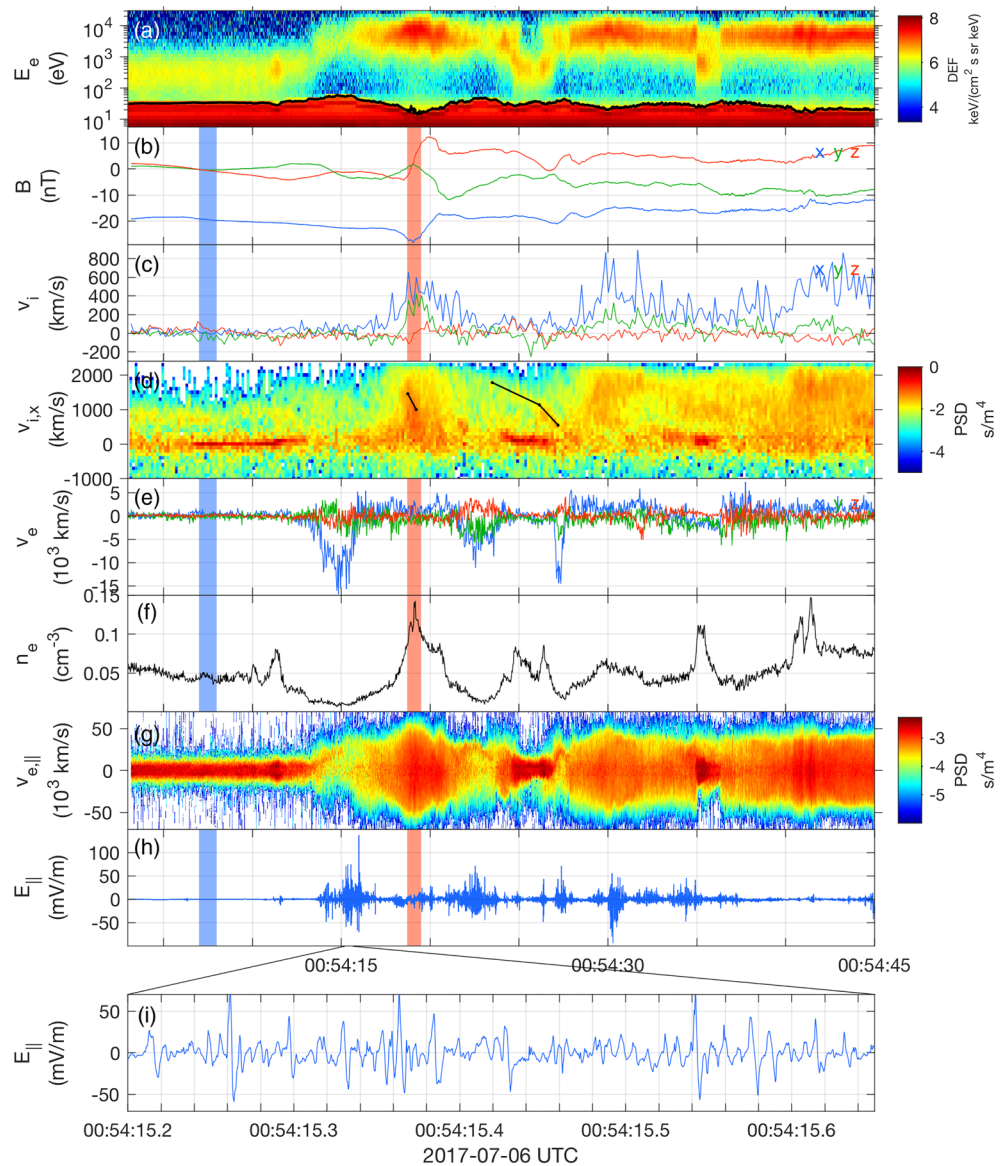
Figure 1. Overview of separatrix crossings. The blue and red shaded areas indicate the time intervals from which we extract lobe and plasma sheet parameters, respectively. (a) Energy spectrogram of electron differential energy flux. The black line shows the spacecraft potential, below which spacecraft photoelectrons are present. (b) Magnetic field. (c) Ion velocity. (d) Reduced ion phase space density distribution, integrated over the directions perpendicular to x_{GSE}. The black lines mark velocity dispersion signatures used to estimate the distances to ion acceleration regions. (e) Electron velocity. (f) Electron density. (g) Reduced electron phase space density distribution, integrated over the directions perpendicular to the magnetic field. (h, i) Parallel electric field.

realistic mass ratios (Lapenta et al., 2010). We shall henceforth refer to the regions of low densities and large amplitude electron flows as acceleration channels.

Figure 1g shows the phase space density (PSD) of the reduced electron distribution projected onto the magnetic field:

$$f_e^{1D}(v_\parallel) = \int_{-\infty}^{-\infty} f_e(v_\parallel, v_{\perp,1}, v_{\perp,2}) dv_{\perp,1} dv_{\perp,2}.$$

Inside the three acceleration channels, we can clearly see the accelerated population for $v_{e\parallel} > 0$. These accelerated populations correspond to electron beams directed toward the magnetic reconnection X line, opposite to the exhaust flow. Such beams are prominent features seen in the separatrix regions in numerical

simulations of magnetic reconnection (e.g., Divin et al., 2012; Egedal et al., 2015; Fujimoto, 2014; Hesse, Norgren, et al., 2018). The reduced distributions presented in the simulations bear strong resemblance to the reduced electron distributions observed by MMS presented here.

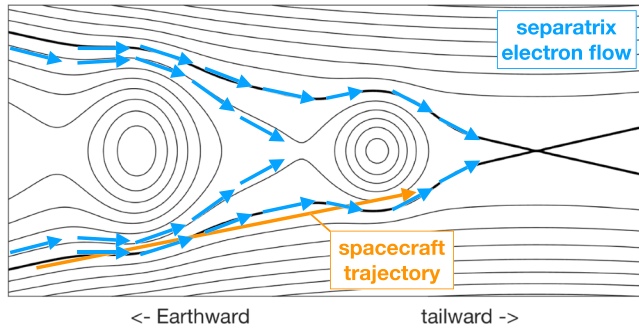All the acceleration channels are found at the edges of the reconnection outflow, where we expect the separatrices to be. Therefore, consistent with numerical simulations, we identify the acceleration channels as being located at the separatrices of a magnetic reconnection site. However, from numerical simulations, we know that density cavities associated with the accelerated populations do not always extend over the whole length of the separatrices (e.g., Egedal et al., 2015). In the case of a guide-field reconnection, the acceleration regions are partially suppressed at two opposing of the four separatrices (e.g., Pritchett & Coroniti, 2004). Therefore, while acceleration channels and reconnection separatrices are closely related, they are not always coincident. Also, importantly, electron acceleration channels are not exclusively related to magnetic reconnection but can occur in a multitude of plasma environments.

Figure 2. Illustration of how the electron flow along the separatrices can be modulated by the formation of flux ropes or successive dipolarization fronts during the magnetic reconnection process. Due to the time-dependent nature of magnetic reconnection, we cannot draw a conclusive magnetic topology and spacecraft trajectory for the entire time interval shown in Figure 1 using only one picture. However, to guide the reader, we have drawn a possible spacecraft trajectory to indicate the repeated crossings of the separatrix and two flux ropes. It must be understood, however, that between the first, second, and third crossings of the separatrix, new islands may have already formed, and the spacecraft are not necessarily located closer to the X line.

Note that our interpretation of the electron flows differ from that of Huang et al. (2019) who suggested that the electron flows could possibly be part of an electron vortex. We agree with their interpretation that the magnetic field structure may be a larger-scale flux rope. However, while it is possible that the flux rope modulates the electron flow, we do not interpret it as an intrinsic feature of the flux rope but rather as adherent to the magnetic reconnection region at large. This is illustrated in Figure 2 that shows a possible magnetic field topology and associated electron flows. Due to the time-dependent nature of magnetic reconnection, we cannot illustrate the entire time interval.

The acceleration channels are associated with large amplitude parallel (Figures 1h and 1i) and perpendicular (shown for a shorter time interval in Figure 6) electric field fluctuations (see also Huang et al., 2019). Since instabilities driven by parallel beams often result in large amplitude parallel electric fields, we will in sections 5 and 6 focus on investigating the relation between the field-aligned electric fields and the parallel streaming populations. First, however, we will quantify in more detail the electron acceleration.

4. Electron Beam Energy

To obtain an estimate of the acceleration potential that the electrons have passed through, we investigate the reduced electron distribution in more detail. Figure 3 again shows the reduced electron distribution, now for a slightly shorter time interval. The thinner black line shows the parallel electron bulk speed $v_{e,||}^{bulk}$, and the thin dashed line shows $v_{e||}^{bulk} \pm v_{te,||}$, where $v_{te,||} = \sqrt{2 k_B T_{e,||}/m_e}$ is the electron thermal speed based on the parallel temperature.

To estimate the electron acceleration inside the acceleration channels, we assume that lobe populations initially at rest have been accelerated to the energies of the observed beams. For each time, the beams are identified as peaks of the phase space density, $v_{beam} = v_{e,||}(f_e = f_{e,max})$. The corresponding energy is given by $e\psi = m_e v_{beam}^2/2$. To avoid picking up the smallest variations in f_e we have first applied a running average over three full 3-D distributions (the averaged distribution in Figure 3 can be compared to the original distribution in Figures 1g or 8a). The obtained speeds v_{beam} are shown as thick solid black lines in Figure 3. We note that the peak phase space densities between the lobe and the acceleration channels are not conserved, $f_e^{lb} > f_e^{beam}$, as indicated by the color in Figure 3 that shifts from dark red in the lobes to light orange inside the first acceleration channel. Due to the presence of electrons generated by plasma-spacecraft interactions (Gershman et al., 2017) at low energies we have used the moments to define the peak phase space density of the lobe $f^{lb} = n_e^{lb}/\pi^{1/2} v_{te}^{lb}$. The decrease in peak phase space density indicates that non-adiabatic processes are at work, for example, wave-particle interaction. Although beam thermalization through wave-particle interaction will decrease the average drift velocity of the beam population, it can initially tend to shift the

peak phase space density to higher energies (see, e.g., Figure 2 in Che et al., 2009). When we find v_{beam}, we therefore exclude times when the peak phase space density of the beam is less than $0.1f^{lb}$. This is, for example, the case during the last part of the first acceleration channel. Note, however, that in section 6 we do study the beam instability for the time interval when $f^{beam} < 0.1f^{lb}$.

The accelerated populations have larger speeds than the moments calculated from the entire distribution, $v_{beam} > v_{e,\parallel}^{bulk}$. This is due to the presence of an additional electron population close to $v_{e,\parallel} = 0$ inside the acceleration channels. Inside the acceleration channels, the temperature (as indicated by the distance between the two dashed lines marking $v_{e,\parallel} \pm v_{te,\parallel}$) is increased relative to the lobes. This initial jump in temperature is also largely due to the presence of the additional population at $v_{e,\parallel} = 0$. The population with low parallel speed could be due to wave-particle interactions, or leakage from the plasma sheet or even the lobes.

The maximum potentials associated with v_{beam} for the three acceleration channels as observed by MMS 1 are $\psi = [1, 800, 2, 400, 1, 400]$ V, respectively (also written on top of Figure 3). We note that MMS 2 and 4 observed a slightly higher value of $\psi = 1, 900$ eV for the third channel. In comparison, characteristic temperatures in the lobe and plasma sheet are $T_e^{lb} = 220$ eV and $T_e^{sh} = 3, 700$ eV (obtained from the blue and red intervals shown in Figure 1). In terms of these characteristic energies, $e\psi \approx [8, 11, 6]\ T_e^{lb} \approx [0.5\ 0.6,\ 0.4]\ T_e^{sh}$. Note that the thermal energy of the plasma sheet is usually larger closer to the neutral sheet (Baumjohann et al., 1989). Because $|\mathbf{B}| > 15$ nT during the entire shown interval, the spacecraft stay relatively close to the plasma sheet boundary layer, and therefore, T_e^{sh} should be considered as a lower bound. The peak phase space density of the beam at maximum v_{beam} for the three channels is $f^{beam}/f^{lb} = [0.13, 0.23, 0.29]$.

We have performed the same analysis as described above for a few other acceleration channels from two days in July 2017, listed in Table 1. The results are shown in Figure 4 (blue circles) as a function of electron beta in the lobe β_e^{lb}. As before, all events we have included from MMS show clear features of a cold population being accelerated through a potential drop. We have not included flat-top distributions, or events in which the entire electron beam has likely been thermalized already: The peak phase space density is as before $> 0.1f^{lb}$. However, all events show evidence of thermalization, f_{beam} at maximum beam energies ψ ranges between 0.1 and 0.3 f^{lb}. It is possible that acceleration channels that are observed close in time to each other can be a single channel that are crossed multiple times (as illustrated in Figure 2). For these MMS events we find that $\psi = 300$–5,500 eV, $e\psi/T_e^{lb} = 1$–17, and $e\psi/T_e^{sh} = 0.1$–1.5. However for the last five acceleration channels in Table 1, T_e^{sh} is likely underestimated, as MMS only skirted the plasma sheet boundary layer. Regardless of this, electrons passing these acceleration channels have already reached a substantial fraction of their final energy before entering the magnetic reconnection exhaust proper. In agreement with previous results obtained by Cluster (Borg et al., 2012; Egedal et al., 2015) (red circles), the acceleration potentials show an inverse dependence on β_e^{lb}. We note that these two studies seem to cover different ranges of β_e^{lb}. This could be due to selection bias, or instrumental differences related to the accuracy to which the densities and temperatures can be determined. Another Cluster study focused on electron flat-top distributions in the magnetic reconnection region in the tail (Asano et al., 2008). They found that in 20% of the cases when
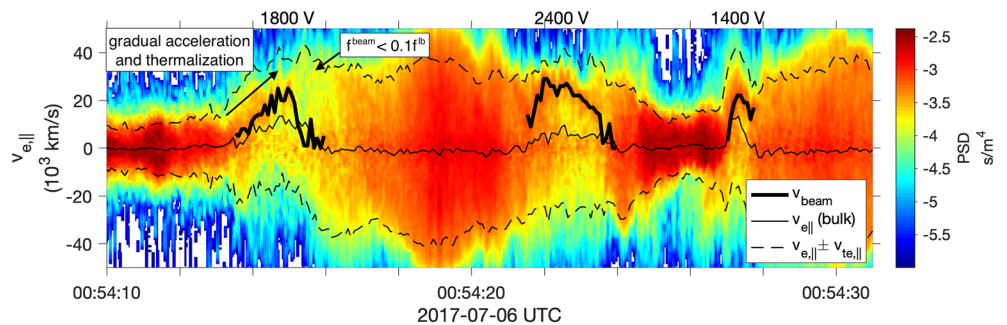
Figure 3. Formation of electron beams as seen from the reduced electron distribution. The intervals show three acceleration channels, where the electron populations are successively shifted toward higher energies. The thicker line follows a local maximum of the phase space density. The energy ψ corresponding to the maximum beam velocity for each channel is written above the respective intervals. The peak phase space density of the beams at these times are $f^{beam}/f^{lb} = [0.13, 0.23, 0.29]$. The solid thin line is the parallel electron bulk speed $v_{e,\parallel}$. The two bounding thin dashed lines mark $v_{e,\parallel} \pm v_{te,\parallel}$.

Table 1
Electron Beam Energy ψ Obtained From Two Days in July 2017

Acceleration channel time interval	ψ (V)	T_e^{lb} (eV)	T_e^{sh} (eV)	β_e^{lb}
2017-07-06T13:54:27.500–54:31.000	1,400	110	1,200	0.005
2017-07-03T21:54:30.300–54:34.100	3,300	270	3,500	0.006
2017-07-03T21:54:35.800–54:42.000	4,100	270	4,600	0.006
2017-07-03T21:55:04.500–55:06.100	2,600	210	4,500	0.007
2017-07-03T21:55:06.500–55:09.200	5,500	210	4,500	0.007
2017-07-03T21:55:11.000–55:13.000	3,100	210	4,500	0.007
2017-07-06T00:54:14.000–54:16.000	1,800	220	3,700	0.010
2017-07-06T00:54:20.300–54:25.000	2,400	330	3,700	0.019
2017-07-06T00:54:25.500–54:29.100	1,400	330	3,700	0.019
2017-07-06T00:55:28.600–55:32.200	300	220	3,400	0.021
2017-07-06T00:55:32.100–55:35.500	1,400	220	3,400	0.021
2017-07-06T00:55:32.300–55:33.500	1,400	220	3,400	0.021
2017-07-06T00:55:38.500–55:43.500	800	220	3,400	0.021
2017-07-06T08:16:37.000–16:40.500	1,300	350	1,100	0.012
2017-07-06T13:54:27.500–54:31.000	1,400	110	1,200	0.005
2017-07-06T14:07:16.800–07:18.000	800	150	1,100	0.005
2017-07-06T14:07:18.500–07:19.700	1,000	150	1,100	0.005
2017-07-06T14:07:19.700–07:22.200	1,000	150	1,100	0.005
2017-07-06T14:07:28.200–07:28.800	1,400	150	1,100	0.005

Note. T_e^{sh} is chosen as the largest temperature observed in the proximity of the acceleration channel. In events where the spacecraft only stay at the edge of the boundary layer, T_e^{sh} is possibly underestimated.
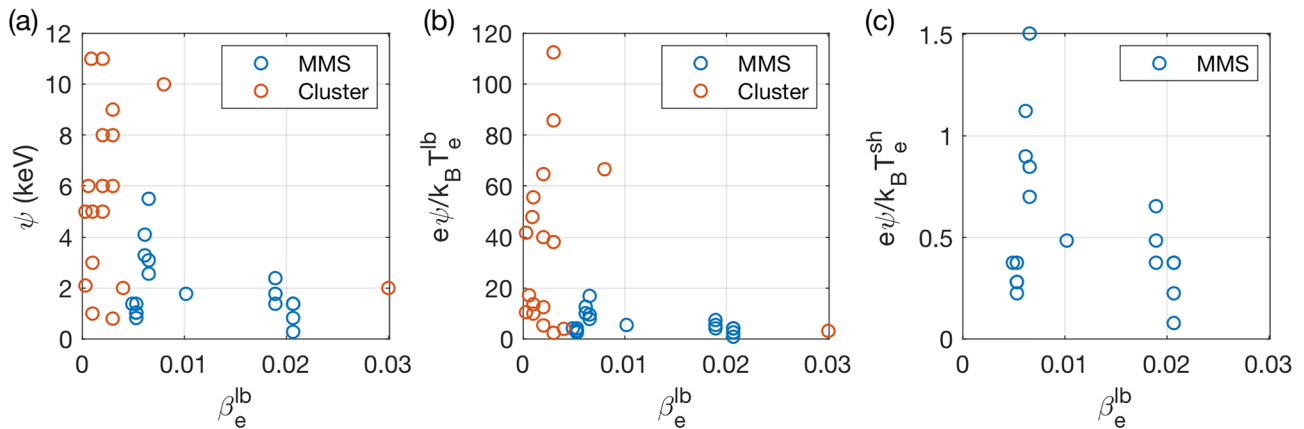
Figure 4. Summary of electron beam energy for a few electron acceleration channels, compared to previous events observed by Cluster (Borg et al., 2012; Egedal et al., 2015). Cluster results are adapted from Table 1 in Egedal et al. (2015). (a) ψ is inversely proportional to β_e^{lb}, and (b) many times the electron thermal energies per charge in the lobe T_e^{lb}/e. (c) $e\psi$ is comparable to plasma sheet thermal energies T_e^{sh}. Note that in events where the spacecraft only stay at the edge of the boundary layer, T_e^{sh} is possibly underestimated, see Table 1.

flat-top distributions were observed in the off-equatorial region, electron beams directed toward the X line were present. The beams had energies of 4–10 keV.

Similar to previous observational studies of both dayside (e.g., Lindstedt et al., 2009; Mozer et al., 2002; Vaivads et al., 2004) and nightside (e.g., Lu et al., 2010; Wang et al., 2012, 2013) magnetic reconnection, the acceleration channels we study in this paper are associated with density cavities. Figure 5a shows the relation between the lobe densities n_e^{lb} and the minimum densities inside the acceleration channels n_e^{sep}. For all events, $n_e^{sep} < n_e^{lb}$. We do not show it here, but for all the events, the densities on the plasma sheet side of

Figure 5. (a) The densities inside acceleration channels, n_e^{sep}, are always lower than the lobe densities n_e^{lb}. (b) The ratio of d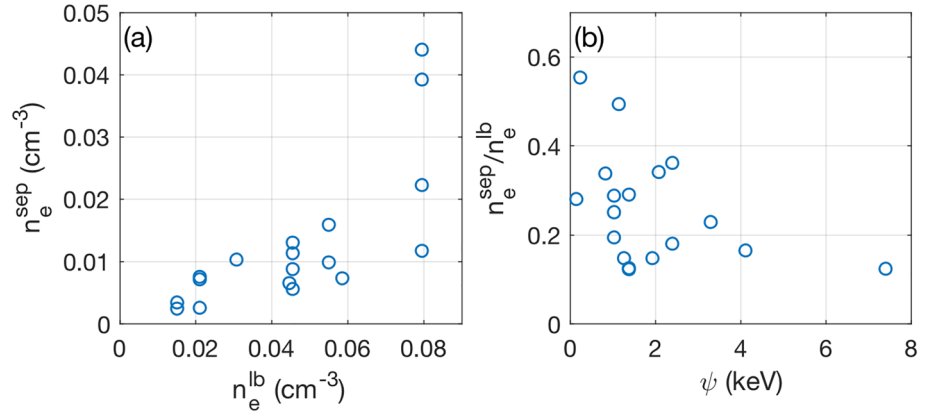ensities between the lobes and acceleration channels, n_e^{sep}/n_e^{lb}, shows an inverse dependence on the beam energy ψ.

the acceleration channels are larger than both n_e^{lb} and n_e^{sep}. Figure 5b shows that the ratio of densities between the lobes and the acceleration channels, n_e^{sep}/n_e^{lb}, becomes smaller with increasing ψ. The decrease in density between the lobe and the acceleration channels is expected from the conservation of phase space density of an accelerated plasma population (e.g., Schamel, 1982). The existence of density cavities at the separatrices is also in agreement with numerical simulations of symmetric antiparallel (e.g., Egedal et al., 2015; Lu et al., 2010; Shay et al., 2001) and guide-field (e.g., Pritchett & Coroniti, 2004) magnetic reconnection. In the case of guide-field reconnection, the reconnection electric field has a component parallel to the magnetic field. This results in enhanced parallel acceleration by the reconnection electric field and larger density cavities at two opposing of the four separatrices. In this study, we have not differentiated between strictly antiparallel and guide-field reconnection. However, since all the events are from the tail, it is likely that any guide field, if present, is low or moderate.

4.1. Width of Acceleration Region

In this section we make a rough estimate of the width of the first acceleration channel in Figure 3, which had a beam energy $\psi = 1,800$ V. For this event, it is not possible to reliably determine the spacecraft trajectory relative to the boundary layer from timing analysis. We therefore take a different approach using the perpendicular electric field. We make the following assumptions: (1) The electron beam is formed by an acceleration potential that is electrostatic in nature. We neglect wave-particle interactions that may have affected the beam, and the beam energy should therefore be considered an upper limit of such an acceleration potential. The parallel potential drop of such an electrostatic potential is accompanied by a perpendicular potential drop. This is consistent with the divergent electric field $E_{\perp,z}$ centered around the electron flow shown in Figures 6a and 6b. We show the original field and the field downsampled to 3 Hz, to highlight the DC variations. We can determine that the field is divergent because MMS cross the southern separatrix from the lobe to the plasma sheet and observes a negative-positive polarity of $E_{\perp,z}$. A divergent electric field is associated with a positive electrostatic potential, consistent with the acceleration of electrons in toward the X line. This can also be seen in numerical simulations of magnetic reconnection (e.g., Figures 4b and 4c in Divin et al., 2012). However, some simulations also show that the electron acceleration along separatrices are in part due to inductive electric fields (Bessho et al., 2015; Egedal et al., 2015). Figure 6c shows the ψ at the original cadence and downsampled to 3 Hz, like the electric field. (2) The perpendicular potential profile of the acceleration channel is Gaussian: $\psi_{\perp}(z) = \psi_0 \exp(-z^2/2l_z^2)$, where z is the coordinate perpendicular to both **B** and the main electron flow $\mathbf{v}_e$, and $\psi_0 = \psi(z = 0)$ is the potential in the center of the acceleration channel. While the Gaussian shape is somewhat arbitrary, we have no way to better determine the exact shape. The perpendicular electric field associated with this potential structure has peak values $|E_z^{max}| = l_z^{-1}\psi_0 \exp(-1/2)$ at $z = \pm l_z$, where the potential is $\psi(z = \pm l_z) = \psi_0 \exp(-1/2)$. The half width is thus given by

$$l_z = \psi(z = \pm l_z)/|E_z^{max}|. \tag{1}$$

We now choose two time steps from where the electric field is the strongest, marked by yellow squares in Figures 6b and 6c. At these times, because the observed electric field maximizes here, the spacecraft are presumably located at an intermediate distance from the center of the acceleration channel, close to l_z. For
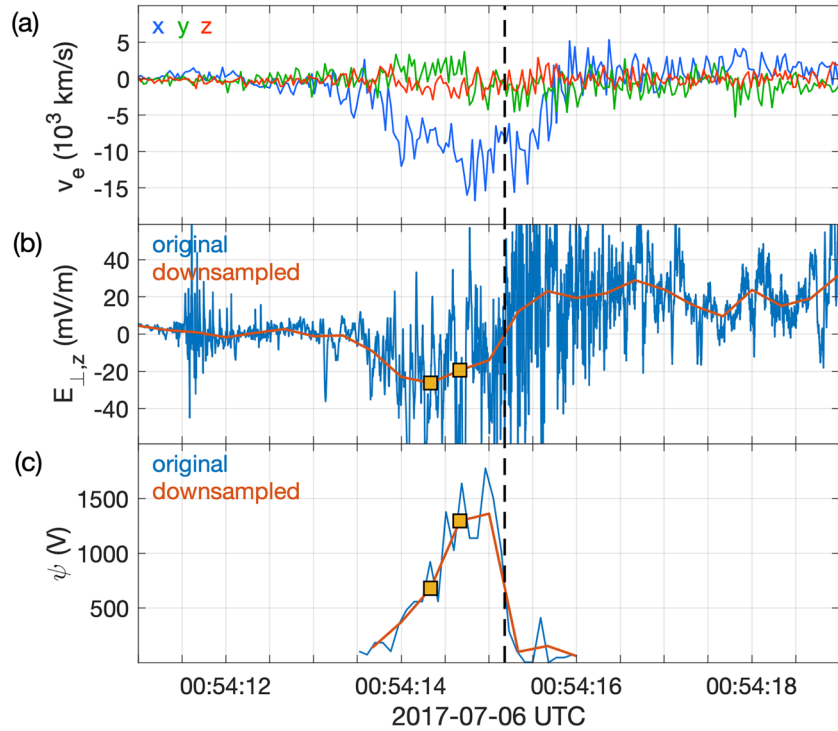
Figure 6. Estimation of acceleration channel thickness using data from MMS 1. (a) Electron flow $\mathbf{v}_e$. (b) Perpendicular electric field $E_{\perp,z}$ at original sampling rate and downsampled to 3 Hz. $E_{\perp,z}$ reverses around the time where $|\mathbf{v}_e|$ is the largest (marked by vertical dashed line). We therefore take the spacecraft to be located at the center of the acceleration channel at this time. (c) Acceleration potential ψ at original cadence and downsampled to 3 Hz. Applying equation (1) to the two times marked by yellow squares, we estimate $l_z \sim 25$–65 km, giving an acceleration channel thickness of 50–130 km.

the two points $|E_z^{max}| = [25, 19]$ mV/m, and $\psi(z = \pm l_z) = [700, 1, 300]$ V, giving estimated half widths $l_z = [25, 65]$ km, respectively. The estimated thickness of the acceleration channel is thus $L = 2l_z = 50$–130 km. In comparison, the ion and electron thermal gyroradii ranges between 100–400 km and 2–8 km, respectively, where the smaller (larger) values are taken at the lobe (sheet) side of the acceleration channel. The Debye length is ~ 0.5 km in the lobes and reaches 4 km inside the acceleration channel. As mentioned in the beginning, the beam energy should be considered as an upper limit of a larger-scale potential structure. Therefore, the acceleration channel thickness we estimated here is also an upper limit estimate.

5. Wave Activity

Inside, and in the vicinity of the acceleration channels, large amplitude parallel electric fields are typically observed. An example is shown in Figure 1i, where the largest amplitude fields form bipolar pulses, often termed electrostatic solitary waves (ESW) (see also Figure 5 in Huang et al., 2019).

To quantify to what extent the electric field can affect the electrons and modify their velocity, it is helpful to look at the sum of the kinetic and potential electron energy in the frame of the wave traveling at speed v_{ph}:

$$U = \frac{m_e}{2}\left(v - v_{ph}\right)^2 - e\phi, \qquad (2)$$

which is a constant of motion. If $U < 0$, the electron is following a trapped trajectory, and if $U > 0$, the electron is following a passing trajectory (Bernstein et al., 1957). The electrons can transition from passing to trapped trajectories (or vice versa) if the wave field is growing (or decaying)—the electrons become trapped (or released). The limiting speeds that separate trapped and passing electron trajectories at the point where the potential is the largest are

$$v(U = 0, \phi = \phi_{max}) = v_{ph} \pm v_{tr}, \qquad (3)$$

where $v_{tr} = \sqrt{2e\phi_{max}/m_e}$ is called the trapping speed. The trapping range defined in equation (3) by the phase speed together with the trapping speed is a good indication of what part of the electron distribution is likely to interact efficiently with the wave electric field.

To find the trapping velocities, we need to find the propagation velocities v_{ph} and electrostatic potentials ϕ of the waves. When the same wave structure is observed by two or more of the spacecraft, we can perform interferometry measurements to obtain the propagating velocity. That is, we measure the delay between the times the structure is observed by the different spacecraft and compare it to the spacecraft separations. This is possible because the spacecraft separation of about 15 km is comparable to the typical length scale of the wave forms $\sim 10\lambda_{De}$, where $\lambda_{De} = (\epsilon_0 k_B T_e/ne^2)^{1/2}$ is the Debye length (Graham, Khotyaintsev, Vaivads, et al., 2016). Inside the acceleration channel $\lambda_{De} = 3.3$ km (using $T_e \sim 2,000$ eV and $n_e = 0.01$ cm^{-3}). Using v_{ph}, we can for each spacecraft obtain the distances between the positive and negative peaks of the bipolar electric fields, which we call the peak-to-peak length scale l_{pp}. If the ESW can be estimated by a Gaussian potential profile, the peak-to-peak length scale is twice the Gaussian half width. The potential of the waves along the trajectory of the spacecraft are calculated by integrating the parallel electric field, using the parallel component of the measured phase velocity, $dl = -v_{ph}dt$:

$$\phi = \int E_\parallel v_{ph} dt.$$

Figure 7 summarizes the properties of the waves that were observed during the first acceleration channel in Figures 1 and 3. Figure 7a shows the obtained phase velocities as a function of the peak-to-peak lengths. The ESWs can roughly be divided into two groups based on their phase speeds, one slower group with $v_{ph} < 5 \times 10^3$ km/s and one faster group with $v_{ph} > 13 \times 10^3$ km/s. Many of the ESWs have significant perpendicular electric fields, which suggests they are three-dimensional structures, with perpendicular length scales comparable to the parallel length scales (Holmes et al., 2018; Steinvall et al., 2019; Tong et al., 2018). If the shape of an ESW were double Gaussian, all four spacecraft would observe the same l_{pp} but potentially different electric fields depending on their relative position perpendicular to the ESW propagation direction. We find that for a single ESW, the four spacecraft observe slightly different l_{pp}. This suggests that the ESWs have non-regular structures, and we therefore show the standard deviation centered on the mean value for each ESW. We find that the peak-to-peak lengths vary between $l_{pp} = 20$ and 120 km with a mean value of $\langle l_{pp} \rangle = 60$ km. Due to different spacecraft locations with respect to the center of the ESWs, as well as irregular shape, the four spacecraft also observe different electric fields and potentials. Figure 7b shows the maximum electrostatic potential ϕ_{max} of each ESW along the spacecraft trajectory as a function of l_{pp}: ϕ_{max} varies between $\phi_{max} = 200$ and $3,400$ V with a mean value of $\langle \phi_{max} \rangle = 1,500$ V. As for the length scales, we show the standard deviation centered on the mean value for each ESW. All potentials are positive, which means that the ESWs correspond to local positive charge densities. Since the majority of them propagated at speeds well above the ion thermal speed, we conclude that they should correspond to depletions of electron density as opposed to clumps of ions. We therefore interpret them as electron phase space holes.

In the interest of comparing the properties of these ESWs to other studies of ESWs, in Figure 7c we also show the potential normalized to the electron thermal energy per charge. While this gives a good first indication of how large part of the electron distribution can be affected by the waves, it does not take into account the speeds of the ESWs like the trapping range defined by equation (3) does. As shown in Figure 7c, $e\phi_{max}/T_e$ varies between $e\phi_{max}/T_e = 0.1$ and 1.1 with a mean value of $\langle e\phi_{max}/T_e \rangle = 0.5$. The peak-to-peak length scale normalized to the Debye length varies between $l_{pp}/\lambda_{De} = 7$ and 32, with a mean value of $\langle l_{pp}/\lambda_{De} \rangle = 16$. Both the length scales and the potentials can be considered comparable (Ergun, Carlson, McFadden, Mozer, Muschietti, et al., 1998) or as representing the upper ranges of values found in previous studies (Cattell et al., 2005; Franz et al., 2005; Graham, Khotyaintsev, Norgren, et al., 2016; Steinvall et al., 2019). However, probe-to-probe interferometry on single spacecrafts, such as done by, for example, FAST (Ergun, Carlson, McFadden, Mozer, Delory, et al., 1998), Polar (Franz et al., 2005), and Cluster (Cattell et al., 2005; Graham, Khotyaintsev, Vaivads, et al., 2016), is limited to resolving speeds below a threshold defined by the separation between the probes and the length scales of the structures (see, e.g., Figure 4b in Graham, Khotyaintsev, Vaivads, et al., 2016). This limitation may have impacted the ranges of speeds, length scales, and therefore potentials possible to characterize in previous studies.

To see how these phase speeds and potentials of the waves compare to the electron distribution in more detail, in Figure 8 we show them in the context of the reduced electron distribution. The black dots show
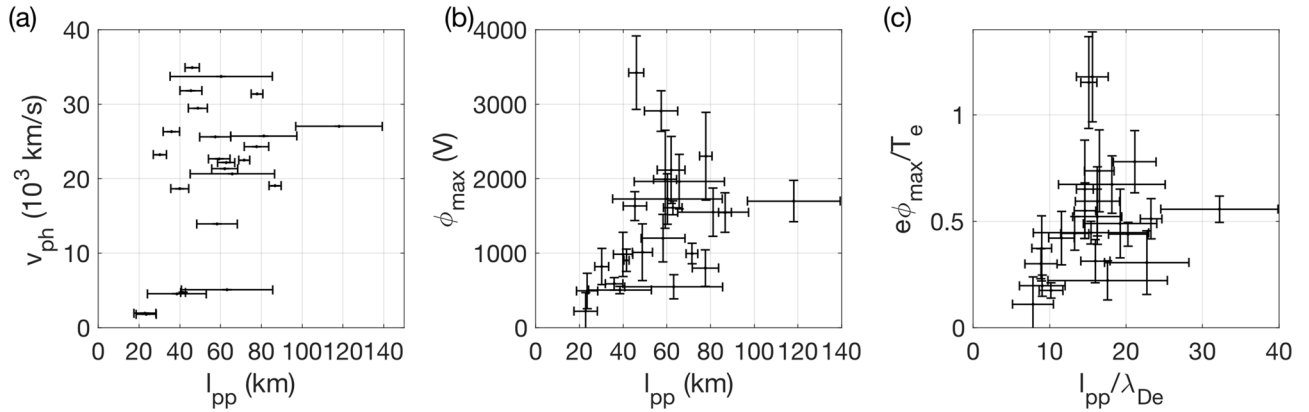
Figure 7. Properties of ESWs observed inside acceleration channel. We show the standard deviation centered on the mean value for each ESW. (a) Phase velocity as a function of peak-to-peak length scale. A large spread in l_{pp}'s between the four spacecraft indicate that an ESW has an irregular shape. (b, c) Electrostatic potential and peak-to-peak length scales of ESWs in unnormalized and dimensionless units. Since each spacecraft can pass through an ESW at different distances from its center , the four spacecraft can observe different ϕ_{max}, respectively. The average values for the entire group of ESWs are $\langle l_{pp} \rangle = 60$ km or $\langle l_{pp}/\lambda_{De} \rangle = 16$, and $\langle \phi_{max} \rangle = 1,500$ V or $\langle e\phi_{max}/T_e \rangle = 0.3$.
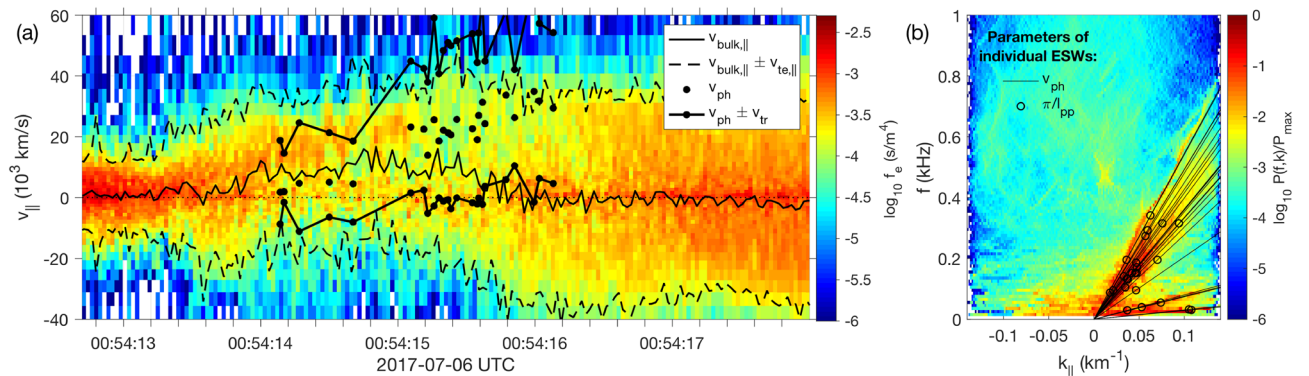

Figure 8. Interaction range of wavefield and electron population. (a) Reduced electron distribution. The lines with dots show the trapping range centered around the phase velocity (black dots). (b) Normalized power of $E_\parallel$ as a function of $k_\parallel$ and f. The lines show the phase velocities of the individual wave structures marked in panel (a). The circles show an estimate of the ESW wavenumber corresponding to a wavelength $\lambda = 2l_{pp}$, $k_\circ = \pi/l_{pp}$.

v_{ph} of individual ESWs, which increase toward the plasma sheet. We find that v_{ph} is loosely proportional to the velocity of the drifting electron population. The trapping ranges $v_{ph} \pm v_{tr}$ (equation (3), based on the maximum ϕ observed by the four spacecraft) are shown as two black lines bounding v_{ph}. At earlier times where $v_{ph} < 5 \times 10^3$ km/s, the trapping range encompasses significant parts of the beam, indicating favorable conditions for strong wave-electron interaction. At later times where $13 \times 10^3 < v_{ph} < 35 \times 10^3$ km/s, the beam is not as apparent and has likely become significantly thermalized. The trapping range encompasses a large part of the electron distribution, including the presumably thermalized beam and part of the plasma sheet population. Where the waves overlap with the plasma sheet population, a distinct asymmetry is seen in the electron distribution: The phase space density for $v_\parallel < 0$ is generally larger than for $v_\parallel > 0$. The region of asymmetrically reduced phase space density roughly overlaps with the trapping range of the waves. The thermalized beam and the asymmetric plasma sheet population, in conjunction with the large trapping ranges, indicate the strong wave-particle interaction that is likely taking place.

Figure 8b shows the spectral representation of the ESWs. The power spectrum of $E_\parallel$ as a function of frequency f and parallel wavenumber $k_\parallel$ is obtained from four-spacecraft interferometry for the time interval shown in Figure 8a. The method is described for two points of measurement by Graham, Khotyaintsev, Vaivads, et al. (2016) but here generalized to four points. This removes the need to assume a given propagation direction. The resolvable $k_\parallel$'s are related to the inter-spacecraft separation as $k_{\parallel,max} = \pi / \max(\Delta l_{ij,\parallel})$, where $\Delta l_{ij,\parallel}$ is the distance between the individual spacecraft pairs (denoted by indices i and j) parallel to the ambient magnetic field. In our case $\max(\Delta l_{ij,\parallel}) = \Delta l_{14,\parallel} = 25$ km, giving $|k_\parallel|_{max} \approx 0.125$ km^{-1}. The lower
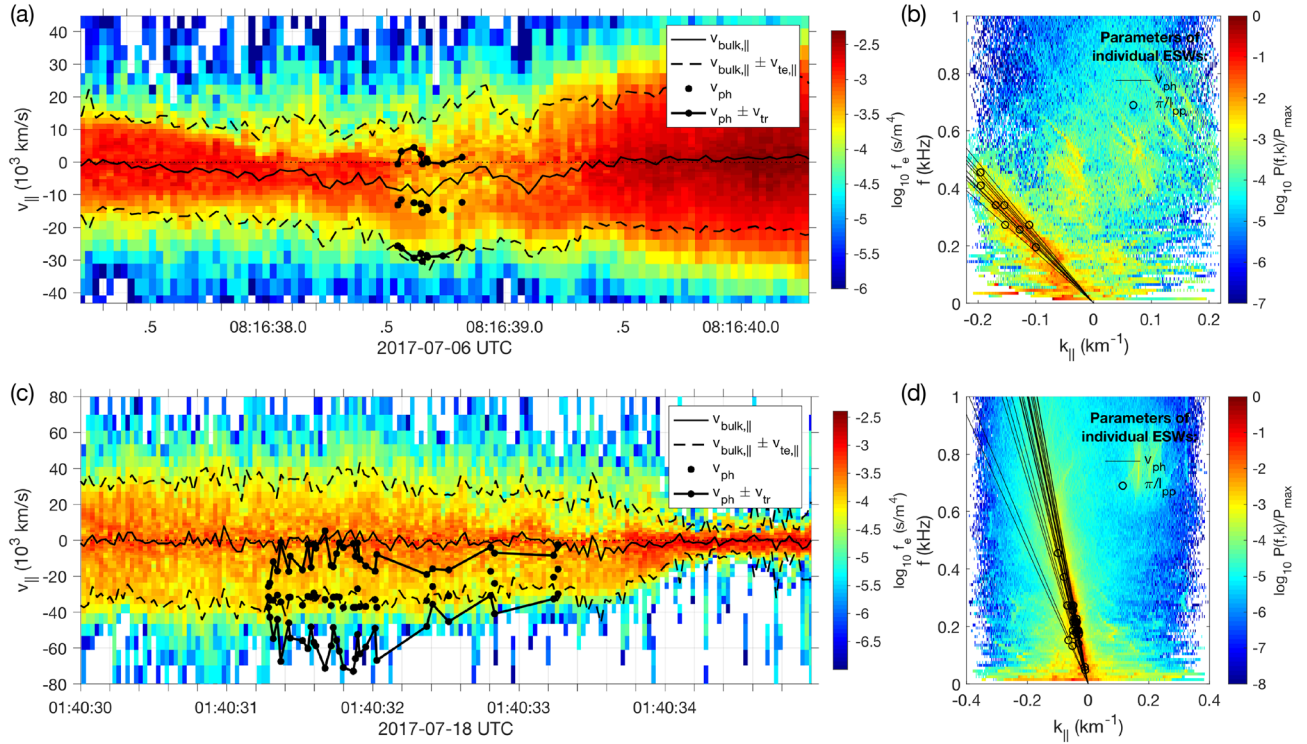
Figure 9. Interaction range of wave electric field and electron population. (a, c) Reduced electron distribution. The lines with dots show the trapping range centered around the phase velocity (black dots). For the first case, the phase speeds v_{ph} are proportional to the beam speed. In the second case, the phase speeds are proportional to the electron thermal speed. For both cases, the interaction ranges $v_{ph} \pm v_{tr}$ cover significant parts of the electron distributions. (b, d) Normalized power of $E_{\parallel}$, as a function of $k_{\parallel}$ and f. The lines show the phase velocities of the individual wave structures marked in panel (a). The circles show an estimate of the central wavenumber $k_o \sim \pi/l_{pp}$ assuming the wavelength is given roughly by $\lambda = 2l_{pp}$.

power found at $k_{\parallel} \lesssim 0.05\,\text{km}^{-1}$ and $f \gtrsim 0.4\,\text{kHz}$ might be due to spatial aliasing. The black lines mark the phase velocity of the individual ESWs (as shown in Figure 8a). In this representation of the wave properties, we can also distinguish that the faster ESWs are represented at higher frequencies than the slower ESWs.

We have performed wave analyses for a number of events and present two more of them in Figure 9. We observe both similarities and differences between the different cases. Figure 9a shows an acceleration channel with a distinct beam, which is included in Table 1 and Figure 4. Again we find that the phase velocities are proportional to the beam speed and that the wave interaction range covers the beam. In contrast, in Figure 9c, although there is an asymmetry in $f_e(v_{\parallel})$ associated with a bulk flow of about 10,000 km/s close to the lobe, no distinct beam is observed. However, the phase velocities are proportional to the thermal speed (dashed line), which increases away from the lobe. The presence of the waves indicate that a beam might have at some point been present in the region. However, since we do not observe any beam, it is possible that such a beam has already been destroyed by the wave-electron interaction and that what we observe is the thermalized beam. This is supported by the fact that the trapping range $v_{ph} \pm v_{tr}$ covers a large part of the electron distribution. This case is similar to the later stages of the beam evolution shown in Figure 8a. Because no distinct beam is observed, this time interval is not included in Table 1 or Figure 4. Figures 9b and 9d show that the phase velocities obtained from timing analysis of individual ESWs correspond well to the maximum wave power in the dispersion relation obtained from four-spacecraft spectral analysis.

6. Spatiotemporal Evolution and Instability Analysis

To investigate whether the observed plasma distributions can account for the generation of the ESWs, we solve the unmagnetized, electrostatic dispersion equation:

$$0 = 1 - \sum_s \frac{\omega_{ps}^2}{k^2 v_{ts}^2} Z'\left(\frac{\omega - k v_{ds}}{k v_{ts}}\right) \tag{4}$$
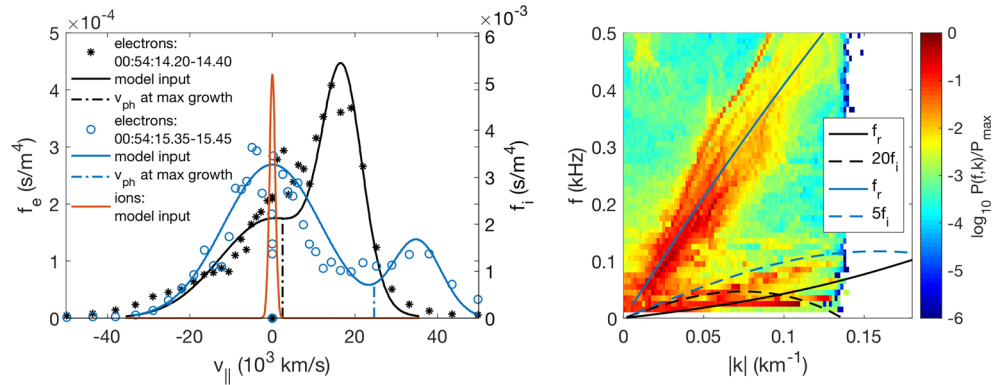
Figure 10. Wave instability analysis. (a) Observed and fitted model distribution during two time intervals corresponding to where the slower (black) and faster (blue) ESWs are observed, respectively. (b) Observed dispersion relation and real (f_r) and imaginary (f_i) frequencies obtained by solving equation (4) for the two distributions in (a). Both solutions show real frequencies corresponding well to the observed ones. For the slow ESWs the range of $k_\parallel$ with positive growth rates $f_r > 0$ corresponds to where the wave power is the largest. For the faster ESWs, the peak growth rate is shifted toward larger $k_\parallel$ or equivalently smaller wavelengths.

for the event presented in Figure 8. Here, Z is the plasma dispersion function, $\omega_{ps} = \sqrt{ne^2/m_s\epsilon_0}$ is the plasma frequency, $v_{ts} = \sqrt{2k_B T_s/m_s}$ is the thermal speed, v_{ds} is the drift speed, and "s" denotes the different plasma populations with mass m_s and temperature T_s. Based on the observed ESW characteristics, the ESWs in Figure 8 could roughly be divided into two groups: One group with lower v_{ph} observed at earlier times and one group with larger v_{ph} observed at later times. We will therefore investigate different combinations of plasma populations.

We expect the accelerated lobe electron population to be the main driver of the instability. This beam, however, can be in different stages of evolution. Further downstream the acceleration channel, our observations and previous simulations (e.g., Egedal et al., 2015) show that the peak phase space density is shifted toward larger speeds but also that the beam is weaker; that is, it has a lower density relative to the electron population at lower speeds (cf. the black stars and blue circles in Figure 10a). To the zeroth order, the shift to larger speed is due to the acceleration. However, the wave-particle interaction can also contribute to this as follows: Electron trapping removes phase space density from the lower speed edge of the beam, decreasing its density and at the same time shifting the beam peak to higher speeds (e.g., Che et al., 2009). Recall that when acquiring the beam energy ψ in section 4, we did not include beams with $f_e^{peak} < 0.1 f_e^{lb}$. The distribution shown with blue circles in Figure 10 is an example of such a distribution that was considered too thermalized. Note that a beam drift speed of 35,000 km/s would correspond to a beam energy of 3,500 eV. The electron population at lower speeds can be plasma sheet electrons that enter the acceleration channel during part of their gyromotion. It can also be the trapped electrons that were originally part of the beam. A large part of the low-velocity electrons are within the trapping range of the ESWs. The ions can be both cold lobe and hotter plasma sheet populations. However, the ion thermal speeds of both lobe and plasma sheet ions are both low in comparison to electron and phase speeds, so in the dispersion analysis we will only consider a single (medium hot) ion population with a temperature of $T_i = 5$ keV, corresponding to a thermal speed of $v_{ti} = 980$ km/s. An ion temperature of 10 keV would correspond to a thermal speed of 1,380 km/s, which is not a significant difference considering the phase speeds and electron speeds.

We consider two different electron distributions, based on observed distributions at slightly earlier (black) and later (blue) times where the observed v_{ph} are slower and faster, respectively (Figure 10a). The solid lines show fits to the 1-D reduced electron distributions (black: $n_e = [0.055, 0.045]$ cm^{-3}, $T_e = [900, 130]$ eV, $v_d = [0, 17, 000]$ km/s, blue: $n_e = [0.080, 0.020]$ cm^{-3}, $T_e = [800, 200]$ eV, $v_d = [0, 35, 000]$ km/s) and are used as input to equation (4). The resulting real and imaginary frequencies $f = f_r + if_i$ obtained from equation (4) are shown overlaid with the observed power distribution in Figure 10b. For both cases we obtain good matches to the real frequencies f_r, while the maximum growth for the faster ESWs are shifted toward higher $k_\parallel$'s. The growth rate for the faster beam is about 10 times larger than that for the slower beam. The phase speeds at maximum growth rate are $v_{ph}^{slow} = 2,500$ km/s and $v_{ph}^{fast} = 27,000$ km/s, respectively, shown as vertical dashed-dotted lines in Figure 10a.

For the slower ESWs, depending on small variations of the input parameters, either the ion-electron or electron-electron modes are dominating. The ion-electron mode is essentially a Buneman type mode with a hot electron background that does not interact with the drifting electron population (Norgren et al., 2015). The slow electron-electron mode is an electron-acoustic wave. The faster ESWs are generated by an electron beam-mode instability with close to constant phase speed regardless of wavenumber. The evolution of instabilities from Buneman to electron beam-mode is similar to what was described by Che et al. (2009) for guide-field reconnection. Although the electron beams we study here are not located inside the EDR, the local dynamics can be the same.

Since we observe large amplitude highly nonlinear localized structures, we are not observing the waves in the linear stage of instability. The predicted growth is therefore not necessarily expected to coincide with the range of $k_\parallel$'s where the linear growth rate maximizes. Although some simulations do show good correspondence between observed wave characteristics and linear instability growth rates (e.g., Chen et al., 2015; Fujimoto, 2006), ESWs are, for example, known to merge with each other and grow in size (e.g., Mottez et al., 1997), which would correspond to a shift to smaller $k_\parallel$'s. If we would assume that the wave power at the initial stages of the beam-mode instability peaked at $0.15 \, \text{km}^{-1}$ but due to coalescence has shifted to $0.05 \, \text{km}^{-1}$, this would correspond to a change from a wavelength $\lambda = 40 \, \text{km}$ to a corresponding length scale of the ESWs of $120 \, \text{km}$. Another effect that may play a role in modifying the wave growth is the velocity shear and the perpendicular structure of the flow channel inside which they grow (Che et al., 2011). For example, in our study, a large range of estimated l_{pp}'s are comparable to the estimated width of the acceleration channel, which was $L \approx 50 - 130 \, \text{km}$. For some of the ESWs, the electric field perpendicular to the ambient magnetic field was comparable or even larger than the parallel field (not shown). This suggests that the perpendicular length scales can be comparable to the parallel length scales (Franz et al., 2000) and in extension to the perpendicular width of the acceleration channel. In such cases, the waves cannot be considered as plane waves with infinite extent in the perpendicular direction, which equation (4) assumes. However, extending the wave analysis to include these effects is beyond the scope of this paper. ESWs are also known to be limited in size by transverse instabilities (Graham, Khotyaintsev, Vaivads, et al., 2016; Muschietti et al., 2000). If the bounce frequency of electrons trapped in the potential well of the ESWs exceeds the gyrofrequency, the ESWs tend to become unstable and dissipate. The bounce frequency for a given potential increases with decreasing length scale or correspondingly larger k's. We have examined this relation here (not shown) and find that the limiting k's are about three times larger than the k's where the wave power maximizes. We therefore do not think this is the deciding factor in determining the range of observed length scales.

7. Discussion

We have investigated the electron acceleration and wave-particle interaction in acceleration channels located at magnetic reconnection separatrices in the magnetotail. Generally, we found that the lobe populations were accelerated up to a significant fraction of the thermal energies in the plasma sheet. In some cases, we specifically observed the gradually electron acceleration, that is, the formation of the electron beam. Nonlinear ESWs that were observed at the same time as the accelerated populations had large enough potentials to interact with a significant part of the electron distribution, including the beam. Here we will discuss how the wave-particle interaction and spatial effects are expected to alter the beam and how the continuous acceleration of the beam can alter the ESWs. We will also discuss how the wave properties can be related to a thermalized beam.

Numerical simulations of magnetic reconnection show that electrostatic waves that initially form at lower phase speeds are often accelerated to larger speeds in close connection with the evolving electron distributions (Che et al., 2009; Fujimoto, 2006, 2014; Huang et al., 2014). While some wave structures merge, the ones that persist are observed continuously. That is, the waves are not initially formed at lower speeds, dissipate, and reformed at higher speeds. Although we are not able to track an individual ESW in our observations, the general trend is consistent with simulations. That is, closer to the lobes (plasma sheet) where the beam speed is lower (higher), the phase speeds of the ESWs are lower (higher). Therefore, the evolutions of ESWs in our observations are likely also continuous. The cojoint evolution of beam and ESWs has been investigated both from the point of view of generating instabilities and self-consistent momentum balance of plasma populations in the presence of ESWs. Che et al. (2009) investigated how the evolving distributions were linearly unstable to different types of instabilities. They showed that the ESWs that first formed due to

the Buneman instability were continuously sustained by the electron two-stream instability. This description is consistent with what we found when investigating the stability of the observed plasma distributions in section 6. Taking a different approach, Hutchinson and Zhou (2016) and Zhou and Hutchinson (2016) investigated in detail the self-consistent momentum balance of ion and electron populations in the presence of EH, which manifest as ESWs in the electric field data. They showed that when an EH accelerates or grows in depth, ion and electron plasma momentum is changed both within the hole and outside, by an energization process they called jetting, which leads to self-acceleration of the EHs. They also demonstrated that, through Galilean relativity, the process transferring momentum to the electron population when an EH was accelerating is equivalent to the situation when it is the electron population that is instead accelerating due to a background force, such as an electric field. That is, the continuously accelerating electron population leads to the acceleration of the EH, and the accelerating EH leads to the acceleration of the electron beam. Of course, this joint acceleration does not occur in an isolated system. There must be a third party from which the momentum is transferred, for example, a second electron population or an ion population. Given such a scenario, an interesting question arises. If the electron population initially accelerated by a background electric field leads to the formation and acceleration of EHs, will the accelerating EHs eventually take over the process and lead to further acceleration of the drifting electrons?

Like mentioned above, for the beam in Figure 8a, the beam thermalization became more prominent when the beam had already been accelerated to larger energies. The point in time when the beam became significantly thermalized coincided roughly with the appearance of high velocity ESWs. It is possible that the increased thermalization could be related to the generating instabilities. The electron beam-mode instability, which we found could be responsible for the wave generation in the region of large v_{ph}'s and beam speed, had a growth rate roughly 10 times larger than the instabilities that were active when the beam had lower speeds. The increased thermalization can also be due to the integrated effect of wave-particle interactions along the acceleration channel. That is, the further down the acceleration channel the beam has progressed, the longer distance the wave-particle interaction has had the time to affect the beam.

We also consider the case where the weakened beam could be partially due to spatial effects perpendicular to the magnetic field. For example, if we assume that the initial lobe population is isotropic, electrons with pitch angles close to 90° would cover a larger perpendicular distance throughout their gyromotion than electrons with pitch angles closer to 0° or 180°. The beam would therefore be weaker at the edges of the acceleration channel than at the center. However, the gyroradii of lobe electrons, based on $T_e^{lb} = 220$ eV and $B^{lb} = 20$ nT, is $\rho_e = 2.5$ km, which is significantly smaller than the estimated thickness of the acceleration channel $L \approx 50$–130 km. For this gyration effect to be important, it is likely that some prior heating and pitch angle scattering would have to had taken place. As shown, one source of such parallel heating is the ESWs. The three-dimensional structure of the ESWs associated with perpendicular electric fields could also contribute to pitch angle scattering, directing parallel motion to perpendicular. Huang et al. (2019) also showed that strong large amplitude lower-hybrid waves were present in the region, which may also play a role in electron pitch angle scattering.

The wave-particle interaction can influence the shape and energy of the electron beam. For example, in a growing wave potential structure, electrons are progressively trapped, and electrons from the lower speed edge of the beam are gradually removed. This beam erosion could spread out the beam in velocity space and shift the peak phase space density of the beam to higher energies (see, e.g., Figure 2 in Che et al., 2009). The speeds of beam electrons that are not trapped will also be modulated by the potential ϕ of the waves. Without complete spatiotemporal information about the wave-particle interaction process, it is impossible to separate the modulating effect of ϕ from the larger-scale separatrix acceleration potential that was discussed in the introduction. In addition, because the beam modulation by the waves occurs at the observed timescale of the ESWs (few milliseconds), which are smaller than the sampling time of FPI (30 ms), the beam modulation is undersampled. The undersampled beam will appear spread out in velocity space resulting in a higher apparent beam temperature and may also shift in energy with respect to a beam that was only affected by a larger-scale potential. Effects such as those mentioned above may have affected the beam energies we measure, as listed in Table 1 and Figure 4.

Given the cojoint evolution of the electron beam and the wave characteristics, is it possible to learn something about the acceleration and/or thermalization solely from the observed wave characteristics? Due to the nature of the generating instabilities, and momentum transfer as described by Hutchinson and Zhou

(2016), the ESW speeds should provide a lower bound of the speed of the electron beam (or remnant thereof). However, the beam speed can be highly influenced by wave-particle interaction, not only acceleration by a background electric field. In Figure 9c, we presented a case where no distinct beam could be observed. The phase speeds were roughly proportional to the electron thermal speed, which both increased away from the lobe, similar to the case in Figure 8a where a distinct beam was observed. Due to the similar wave behavior between the cases with and without distinct beams, we believe that the beam in the latter case had already been completely thermalized. Given the discussion above, the phase speeds should provide an estimate of the remnant beam component, which in turn could provide an upper limit of the bulk acceleration of a lobe population.

8. Conclusions

In this study we investigated the electron acceleration and subsequent wave generation and wave-particle interaction at magnetic reconnection separatrices in the magnetotail. We summarize our conclusions below.

- Adjacent to the reconnection exhaust, we found relatively thin regions of electron lobe populations accelerated toward the X line. The electrons were accelerated to energies of 300–5,500 eV, several times the thermal energies within the lobe, and a significant fraction of the thermal energies inside the outflow.
- All acceleration regions were associated with density cavities. The difference in densities between the lobes and the acceleration channels increased with increasing electron beam energy, consistent with theoretical predictions.
- For two acceleration channels presented in more detail, we could observe how the lobe populations were gradually accelerated. For one of them, the resulting beam became significantly weaker closer to the plasma sheet.
- Electrostatic solitary waves observed in the acceleration regions had phase speeds proportional to the beam speeds. The potentials of the waves were large enough such that the waves could interact efficiently with a large part of the electron population, including the beam. This indicates that the waves play an important role in controlling the evolution of the beam, aiding to thermalize it.
- For one acceleration channel we investigated the instability of the evolving electron distribution and found that it could account for the observed wave properties. When the beam had been accelerated to moderate speeds, it was unstable to a combination of competing Buneman and electron-acoustic instabilities, generating waves at low phase speeds. When the beam had been accelerated to larger speeds and had become weaker, the distribution was unstable to an electron beam-mode instability, generating waves at larger speeds.

Our study shows that field-aligned electrostatic waves can efficiently convert electron drift into thermal energy of the plasma. These results are applicable not only to magnetic reconnection but also to any process or environment in which superthermal electron beams form.

References

Asano, Y., Nakamura, R., Shinohara, I., Fujimoto, M., Takada, T., Baumjohann, W., et al. (2008). Electron flat-top distributions around the magnetic reconnection region. *Journal of Geophysical Research*, *113*, A01207. https://doi.org/10.1029/2007JA012461

Baumjohann, W., Paschmann, G., & Cattell, C. A. (1989). Average plasma properties in the central plasma sheet. *Journal of Geophysical Research*, *94*, 6597–6606. https://doi.org/10.1029/JA094iA06p06597

Bernstein, I. B., Greene, J. M., & Kruskal, M. D. (1957). Exact nonlinear plasma oscillations. *Physical Review*, *108*, 546–550. https://doi.org/10.1103/PhysRev.108.546

Bessho, N., Chen, L.-J., Germaschewski, K., & Bhattacharjee, A. (2015). Electron acceleration by parallel and perpendicular electric fields during magnetic reconnection without guide field. *Journal of Geophysical Research: Space Physics*, *120*, 9355–9367. https://doi.org/10.1002/2015JA021548

Borg, A. L., Taylor, M. G. G. T., & Eastwood, J. P. (2012). Observations of magnetic flux ropes during magnetic reconnection in the Earth's magnetotail. *Annales Geophysicae*, *30*, 761–773. https://doi.org/10.5194/angeo-30-761-2012

Cattell, C., Dombeck, J., Wygant, J., Drake, J. F., Swisdak, M., Goldstein, M. L., et al. (2005). Cluster observations of electron holes in association with magnetotail reconnection and comparison to simulations. *Journal of Geophysical Research*, *110*, A01211. https://doi.org/10.1029/2004JA010519

Che, H., Drake, J. F., Swisdak, M., & Yoon, P. H. (2009). Nonlinear development of streaming instabilities in strongly magnetized plasma. *Physical Review Letters*, *102*, 145004. https://doi.org/10.1103/PhysRevLett.102.145004

Che, H., Goldman, M. V., & Newman, D. L. (2011). Buneman instability in a magnetized current-carrying plasma with velocity shear. *Physics of Plasmas*, *18*(5), 052109. https://doi.org/10.1063/1.3590879

Chen, L.-J., Bhattacharjee, A., Puhl-Quinn, P. A., Yang, H., Bessho, N., Imada, S., et al. (2008). Observation of energetic electrons within magnetic islands. *Nature Physics*, *4*, 19–23. https://doi.org/10.1038/nphys777

Chen, Y., Fujimoto, K., Xiao, C., & Ji, H. (2015). Plasma waves around separatrix in collisionless magnetic reconnection with weak guide field. *Journal of Geophysical Research: Space Physics*, *120*, 6309–6319. https://doi.org/10.1002/2015JA021267

Divin, A., Lapenta, G., Markidis, S., Newman, D. L., & Goldman, M. V. (2012). Numerical simulations of separatrix instabilities in collisionless magnetic reconnection. *Physics of Plasmas*, *19*(4), 042110. https://doi.org/10.1063/1.3698621

Drake, J. F., Swisdak, M., Che, H., & Shay, M. A. (2006). Electron acceleration from contracting magnetic islands during reconnection. *Nature*, *443*(7111), 553–556. https://doi.org/10.1038/nature05116

Eastwood, J. P., Goldman, M. V., Hietala, H., Newman, D. L., Mistry, R., & Lapenta, G. (2015). Ion reflection and acceleration near magnetotail dipolarization fronts associated with magnetic reconnection. *Journal of Geophysical Research: Space Physics*, *120*, 511–525. https://doi.org/10.1002/2014JA020516

Egedal, J., Daughton, W., Le, A., & Borg, A. L. (2015). Double layer electric fields aiding the production of energetic flat-top distributions and superthermal electrons within magnetic reconnection exhausts. *Physics of Plasmas*, *22*(10), 101208. https://doi.org/10.1063/1.4933055

Egedal, J., Fox, W., Katz, N., Porkolab, M., Øieroset, M., Lin, R. P., et al. (2008). Evidence and theory for trapped electrons in guide field magnetotail reconnection. *Journal of Geophysical Research*, *113*, A12207. https://doi.org/10.1029/2008JA013520

Egedal, J., Øieroset, M., Fox, W., & Lin, R. P. (2005). In situ discovery of an electrostatic potential, trapping electrons and mediating fast reconnection in the Earth's magnetotail. *Physical Review Letters*, *94*(2), 025006. https://doi.org/10.1103/PhysRevLett.94.025006

Ergun, R. E., Andersson, L., Tao, J., Angelopoulos, V., Bonnell, J., McFadden, J. P., et al. (2009). Observations of double layers in Earth's plasma sheet. *Physical Review Letters*, *102*(15), 155,002. https://doi.org/10.1103/PhysRevLett.102.155002

Ergun, R. E., Carlson, C. W., McFadden, J. P., Mozer, F. S., Delory, G. T., Peria, W., et al. (1998). FAST satellite observations of large-amplitude solitary structures. *Geophysical Research Letters*, *25*, 2041–2044. https://doi.org/10.1029/98GL00636

Ergun, R. E., Carlson, C. W., McFadden, J. P., Mozer, F. S., Muschietti, L., Roth, I., & Strangeway, R. J. (1998). Debye-scale plasma structures associated with magnetic-field-aligned electric fields. *Physical Review Letters*, *81*, 826–829. https://doi.org/10.1103/PhysRevLett.81.826

Ergun, R. E., Goodrich, K. A., Wilder, F. D., Ahmadi, N., Holmes, J. C., Eriksson, S., et al. (2018). Magnetic reconnection, turbulence, and particle acceleration: Observations in the Earth's magnetotail. *Geophysical Research Letters*, *45*, 3338–3347. https://doi.org/10.1002/2018GL076993

Ergun, R. E., Tucker, S., Westfall, J., Goodrich, K. A., Malaspina, D. M., Summers, D., et al. (2014). *The axial double probe and fields signal processing for the MMS mission* (Vol. 199, pp. 167–188). https://doi.org/10.1007/s11214-014-0115-x

Eriksson, E., Vaivads, A., Alm, L., Graham, D. B., Khotyaintsev, Y. V., & André, M. (2020). Electron acceleration in a magnetotail reconnection outflow region using magnetospheric multiscale data. *Geophysical Research Letters*, *47*, E85080. https://doi.org/10.1029/2019GL085080

Eriksson, E., Vaivads, A., Graham, D. B., Divin, A., Khotyaintsev, Y. V., Yordanova, E., et al. (2018). Electron energization at a reconnecting magnetosheath current sheet. *Geophysical Research Letters*, *45*, 8081–8090. https://doi.org/10.1029/2018GL078660

Fermi, E. (1949). On the origin of the cosmic radiation. *Physical Review*, *75*, 1169–1174. https://doi.org/10.1103/PhysRev.75.1169

Franz, J. R., Kintner, P. M., Pickett, J. S., & Chen, L.-J. (2005). Properties of small-amplitude electron phase-space holes observed by polar. *Journal of Geophysical Research*, *110*, A09212. https://doi.org/10.1029/2005JA011095

Franz, J. R., Kintner, P. M., Seyler, C. E., Pickett, J. S., & Scudder, J. D. (2000). On the perpendicular scale of electron phase-space holes. *Geophysical Research Letters*, *27*, 169. https://doi.org/10.1029/1999GL010733

Fu, H. S., Khotyaintsev, Y. V., André, M., & Vaivads, A. (2011). Fermi and betatron acceleration of suprathermal electrons behind dipolarization fronts. *Geophysical Research Letters*, *38*, L16104. https://doi.org/10.1029/2011GL048528

Fu, H. S., Xu, Y., Vaivads, A., & Khotyaintsev, Y. V. (2019). Super-efficient electron acceleration by an isolated magnetic reconnection. *The Astrophysical Journal*, *870*(2), L22. https://doi.org/10.3847/2041-8213/aafa75

Fujimoto, K. (2006). Time evolution of the electron diffusion region and the reconnection rate in fully kinetic and large system. *Physics of Plasmas*, *13*(7), 072904. https://doi.org/10.1063/1.2220534

Fujimoto, K. (2014). Wave activities in separatrix regions of magnetic reconnection. *Geophysical Research Letters*, *41*, 2721–2728. https://doi.org/10.1002/2014GL059893

Gershman, D. J., Avanov, L. A., Boardsen, S. A., Dorelli, J. C., Gliese, U., Barrie, A. C., et al. (2017). Spacecraft and instrument photoelectrons measured by the dual electron spectrometers on MMS. *Journal of Geophysical Research: Space Physics*, *122*, 11,548–11,558. https://doi.org/10.1002/2017JA024518

Graham, D. B., Khotyaintsev, Y. V., Norgren, C., Vaivads, A., André, M., Lindqvist, P.-A., et al. (2016). Electron currents and heating in the ion diffusion region of asymmetric reconnection. *Geophysical Research Letters*, *43*, 4691–4700. https://doi.org/10.1002/2016GL068613

Graham, D. B., Khotyaintsev, Y. V., Vaivads, A., & André, M. (2015). Electrostatic solitary waves with distinct speeds associated with asymmetric reconnection. *Geophysical Research Letters*, *42*, 215–224. https://doi.org/10.1002/2014GL062538

Graham, D. B., Khotyaintsev, Y. V., Vaivads, A., & André, M. (2016). Electrostatic solitary waves and electrostatic waves at the magnetopause. *Journal of Geophysical Research: Space Physics*, *121*, 3069–3092. https://doi.org/10.1002/2015JA021527

Hesse, M., Liu, Y.-H., Chen, L.-J., Bessho, N., Wang, S., Burch, J. L., et al. (2018). The physical foundation of the reconnection electric field. *Physics of Plasmas*, *25*(3), 032901. https://doi.org/10.1063/1.5021461

Hesse, M., Norgren, C., Tenfjord, P., Burch, J. L., Liu, Y.-H., Chen, L.-J., et al. (2018). On the role of separatrix instabilities in heating the reconnection outflow region. *Physics of Plasmas*, *25*(12), 122902. https://doi.org/10.1063/1.5054100

Holmes, J. C., Ergun, R. E., Newman, D. L., Ahmadi, N., Andersson, L., Le Contel, O., et al. (2018). Electron phase-space holes in three dimensions: Multispacecraft observations by magnetospheric multiscale. *Journal of Geophysical Research: Space Physics*, *123*, 9963–9978. https://doi.org/10.1029/2018JA025750

Hoshino, M., Mukai, T., Terasawa, T., & Shinohara, I. (2001). Suprathermal electron acceleration in magnetic reconnection. *Journal of Geophysical Research*, *106*, 25,979–25,998. https://doi.org/10.1029/2001JA900052

Huang, S. Y., Jiang, K., Yuan, Z. G., Zhou, M., Sahraoui, F., Fu, H. S., et al. (2019). Observations of flux ropes with strong energy dissipation in the magnetotail. *Geophysical Research Letters*, *46*, 580–589. https://doi.org/10.1029/2018GL081099

Huang, C., Lu, Q., Wang, P., Wu, M., & Wang, S. (2014). Characteristics of electron holes generated in the separatrix region during antiparallel magnetic reconnection. *Journal of Geophysical Research: Space Physics*, *119*, 6445–6454. https://doi.org/10.1002/2014JA019991

Huang, S. Y., Vaivads, A., Khotyaintsev, Y. V., Zhou, M., Fu, H. S., Retinò, A., et al. (2012). Electron acceleration in the reconnection diffusion region: Cluster observations. *Geophysical Research Letters*, *39*, L11103. https://doi.org/10.1029/2012GL051946

Hutchinson, I. H., & Zhou, C. (2016). Plasma electron hole kinematics. I. Momentum conservation. *Physics of Plasmas*, *23*(8), 082101. https://doi.org/10.1063/1.4959870

Khotyaintsev, Y. V., Graham, D. B., Steinvall, K., Alm, L., Vaivads, A., Johlander, A., et al. (2020). Electron heating by Debye-scale turbulence in guide-field reconnection. *Physical Review Letters*, *124*, 045,101. https://doi.org/10.1103/PhysRevLett.124.045101

Lapenta, G., Markidis, S., Divin, A., Goldman, M., & Newman, D. (2010). Scales of guide field reconnection at the hydrogen mass ratio. *Physics of Plasmas*, *17*(8), 082106. https://doi.org/10.1063/1.3467503

Lindqvist, P.-A., Olsson, G., Torbert, R. B., King, B., Granoff, M., Rau, D., et al. (2014). The spin-plane double probe electric field instrument for MMS. *Space Science Reviews*, *199*, 137–165. https://doi.org/10.1007/s11214-014-0116-9

Lindstedt, T., Khotyaintsev, Y. V., Vaivads, A., André, M., Fear, R. C., Lavraud, B., et al. (2009). Separatrix regions of magnetic reconnection at the magnetopause. *Annales Geophysicae*, *27*(10), 4039–4056. https://doi.org/10.5194/angeo-27-4039-2009

Lu, Q., Huang, C., Xie, J., Wang, R., Wu, M., Vaivads, A., & Wang, S. (2010). Features of separatrix regions in magnetic reconnection: Comparison of 2-D particle-in-cell simulations and Cluster observations. *Journal of Geophysical Research*, *115*, A11208. https://doi.org/10.1029/2010JA015713

Mottez, F., Perraut, S., Roux, A., & Louarn, P. (1997). Coherent structures in the magnetotail triggered by counterstreaming electron beams. *Journal of Geophysical Research*, *102*, 11,399–11,408. https://doi.org/10.1029/97JA00385

Mozer, F. S., Agapitov, O. V., Giles, B., & Vasko, I. (2018). Direct observation of electron distributions inside millisecond duration electron holes. *Physical Review Letters*, *121*, 135102. 121.135102

Mozer, F. S., Bale, S. D., & Phan, T. D. (2002). Evidence of diffusion regions at a subsolar magnetopause crossing. *Physical Review Letters*, *89*(1), 015002. https://doi.org/10.1103/PhysRevLett.89.015002

Muschietti, L., Roth, I., Carlson, C. W., & Ergun, R. E. (2000). Transverse instability of magnetized electron holes. *Physical Review Letters*, *85*, 94. https://doi.org/10.1103/PhysRevLett.85.94

Nagai, T., Shinohara, I., Fujimoto, M., Hoshino, M., Saito, Y., Machida, S., & Mukai, T. (2001). Geotail observations of the Hall current system: Evidence of magnetic reconnection in the magnetotail. *Journal Geophysical Research*, *106*, 25,929–25,950. https://doi.org/10.1029/2001JA900038

Nagai, T., Shinohara, I., Fujimoto, M., Machida, S., Nakamura, R., Saito, Y., & Mukai, T. (2003). Structure of the Hall current system in the vicinity of the magnetic reconnection site. *Journal of Geophysical Research*, *108*(A10), 1357. https://doi.org/10.1029/2003JA009900

Norgren, C., André, M., Graham, D. B., Khotyaintsev, Y. V., & Vaivads, A. (2015). Slow electron holes in multicomponent plasmas. *Geophysical Research Letters*, *42*, 7264–7272. https://doi.org/10.1002/2015GL065390

Northrop, T. G. (1963). Adiabatic charged-particle motion. *Reviews of Geophysics and Space Physics*, *1*, 283–304. https://doi.org/10.1029/RG001i003p00283

Øieroset, M., Lin, R. P., Phan, T. D., Larson, D. E., & Bale, S. D. (2002). Evidence for electron acceleration up to ∼300 keV in the magnetic reconnection diffusion region of Earth's magnetotail. *Physical Review Letters*, *89*(19), 195001. https://doi.org/10.1103/PhysRevLett.89.195001

Øieroset, M., Phan, T. D., Fujimoto, M., Lin, R. P., & Lepping, R. P. (2001). In situ detection of collisionless reconnection in the Earth's magnetotail. *Nature*, *412*, 414–417. https://doi.org/10.1038/35086520

Omura, Y., Matsumoto, H., Miyake, T., & Kojima, H. (1996). Electron beam instabilities as generation mechanism of electrostatic solitary waves in the magnetotail. *Journal of Geophysical Research*, *101*, 2685–2698. https://doi.org/10.1029/95JA03145

Phan, T. D., Shay, M. A., Gosling, J. T., Fujimoto, M., Drake, J. F., Paschmann, G., et al. (2013). Electron bulk heating in magnetic reconnection at Earth's magnetopause: Dependence on the inflow Alfvén speed and magnetic shear. *Geophysical Research Letters*, *40*, 4475–4480. https://doi.org/10.1002/grl.50917

Pollock, C., Moore, T., Jacques, A., Burch, J., Gliese, U., Saito, Y., et al. (2016). Fast plasma investigation for magnetospheric multiscale. *Space Science Reviews*, *199*, 331–406. https://doi.org/10.1007/s11214-016-0245-4

Pritchett, P. L. (2008). Energetic electron acceleration during multi-island coalescence. *Physics of Plasmas*, *15*(10), 102105. https://doi.org/10.1063/1.2996321

Pritchett, P. L., & Coroniti, F. V. (2004). Three-dimensional collisionless magnetic reconnection in the presence of a guide field. *Journal of Geophysical Research*, *109*, A01220. https://doi.org/10.1029/2003JA009999

Russell, C. T., Anderson, B. J., Baumjohann, W., Bromund, K. R., Dearborn, D., Fischer, D., et al. (2014). *The Magnetospheric Multiscale magnetometers* (Vol. 199, pp. 189–256). https://doi.org/10.1007/s11214-014-0057-3

Schamel, H. (1982). Kinetic theory of phase space vortices and double layers. *Physica Scripta T*, *2A*, 228–237,. https://doi.org/10.1088/0031-8949/1982/T2A/030

Shay, M. A., Drake, J. F., Rogers, B. N., & Denton, R. E. (2001). Alfvénic collisionless magnetic reconnection and the Hall term. *Journal of Geophysical Research*, *106*, 3759–3772. https://doi.org/10.1029/1999JA001007

Steinvall, K., Khotyaintsev, Y. V., Graham, D. B., Vaivads, A., Lindqvist, P.-A., Russell, C. T., & Burch, J. L. (2019). Multispacecraft analysis of electron holes. *Geophysical Research Letters*, *46*, 55–63. https://doi.org/10.1029/2018GL080757

Tenfjord, P., Hesse, M., Norgren, C., Spinnangr, S. F., & Kolstø, H. (2019). The impact of oxygen on the reconnection rate. *Geophysical Research Letters*, *46*, 6195–6203. https://doi.org/10.1029/2019GL082175

Toledo-Redondo, S., André, M., Khotyaintsev, Y. V., Lavraud, B., Vaivads, A., Graham, D. B., et al. (2017). Energy budget and mechanisms of cold ion heating in asymmetric magnetic reconnection. *Journal of Geophysical Research: Space Physics*, *122*, 9396–9413. https://doi.org/10.1002/2017JA024553

Tong, Y., Vasko, I., Mozer, F. S., Bale, S. D., Roth, I., Artemyev, A. V., et al. (2018). Simultaneous multispacecraft probing of electron phase space holes. *Geophysical Research Letters*, *45*, 11,513–11,519. https://doi.org/10.1029/2018GL079044

Torbert, R. B., Burch, J. L., Phan, T. D., Hesse, M., Argall, M. R., Shuster, J., et al. (2018). Electron-scale dynamics of the diffusion region during symmetric magnetic reconnection in space. *Science*, *362*(6421), 1391–1395. https://doi.org/10.1126/science.aat2998

Uzdensky, D. A., & Kulsrud, R. M. (2006). Physical origin of the quadrupole out-of-plane magnetic field in hall-magnetohydrodynamic reconnection. *Physics of Plasmas*, *13*(6), 062305. https://doi.org/10.1063/1.2209627

Vaivads, A., André, M., Buchert, S. C., Wahlund, J.-E., Fazakerley, A. N., & Cornilleau-Wehrlin, N. (2004). Cluster observations of lower hybrid turbulence within thin layers at the magnetopause. *Geophysical Research Letters*, *31*, L03804. https://doi.org/10.1029/2003GL018142

Vaivads, A., Retinò, A., Khotyaintsev, Y. V., & André, M. (2011). Suprathermal electron acceleration during reconnection onset in the magnetotail. *Annales Geophysicae*, *29*, 1917–1925. https://doi.org/10.5194/angeo-29-1917-2011

Viberg, H., Khotyaintsev, Y. V., Vaivads, A., André, M., & Pickett, J. S. (2013). Mapping HF waves in the reconnection diffusion region. *Geophysical Research Letters*, *40*, 1032–1037. https://doi.org/10.1002/grl.50227

Wang, S., Chen, L.-J., Bessho, N., Hesse, M., Yoo, J., Yamada, M., et al. (2018). Energy conversion and partition in the asymmetric reconnection diffusion region. *Journal of Geophysical Research: Space Physics*, *123*, 8185–8205. https://doi.org/10.1029/2018JA025519

Wang, R., Du, A., Nakamura, R., Lu, Q., Khotyaintsev, Y. V., Volwerk, M., et al. (2013). Observation of multiple sub-cavities adjacent to single separatrix. *Geophysical Research Letters*, *40*, 2511–2517. https://doi.org/10.1002/grl.50537

Wang, R., Lu, Q., Khotyaintsev, Y. V., Volwerk, M., Du, A., Nakamura, R., et al. (2014). Observation of double layer in the separatrix region during magnetic reconnection. *Geophysical Research Letters*, *41*, 4851–4858. https://doi.org/10.1002/2014GL061157

Wang, R., Nakamura, R., Lu, Q., Du, A., Zhang, T., Baumjohann, W., et al. (2012). Asymmetry in the current sheet and secondary magnetic flux ropes during guide field magnetic reconnection. *Journal of Geophysical Research*, *117*, A07223. https://doi.org/10.1029/2011JA017384

Zhou, C., & Hutchinson, I. H. (2016). Plasma electron hole kinematics. II. Hole tracking particle-in-cell simulation. *Physics of Plasmas*, *23*(8), 082102. https://doi.org/10.1063/1.4959871